Versatile apparatus for attosecond metrology and spectroscopy

M. Fieß, M. Schultze, E. Goulielmakis, B. Dennhardt, J. Gagnon, M. Hofstetter, R. Kienberger, and F. Krausz

Citation: Review of Scientific Instruments **81**, 093103 (2010); doi: 10.1063/1.3475689
View online: https://doi.org/10.1063/1.3475689
View Table of Contents: http://aip.scitation.org/toc/rsi/81/9
Published by the American Institute of Physics

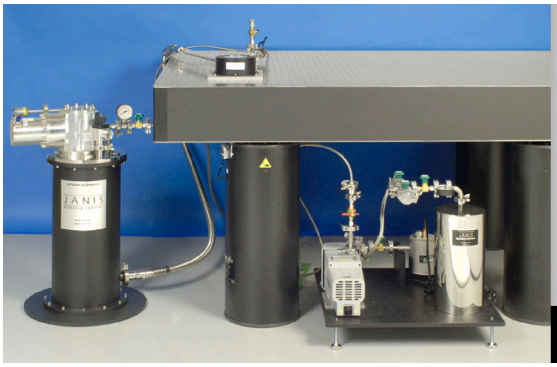

Versatile apparatus for attosecond metrology and spectroscopy

M. Fieß,[1,a] M. Schultze,[1,2] E. Goulielmakis,[1] B. Dennhardt,[3] J. Gagnon,[1] M. Hofstetter,[1] R. Kienberger,[1,3] and F. Krausz[1,2]
[1]*Max-Planck-Institut für Quantenoptik, Hans-Kopfermann-Straße 1, 85748 Garching, Germany*
[2]*Fakultät für Physik, Ludwig-Maximilians-Universität München, Am Coulombwall 1, 85748 Garching, Germany*
[3]*Physik Department E11, Technische Universität München, James-Franck-Straße, 85748 Garching, Germany*

(Received 10 May 2010; accepted 15 July 2010; published online 14 September 2010)

We present the AS-2 Attosecond Beamline at the Joint Laboratory for Attosecond Physics of the Max-Planck-Institut für Quantenoptik and Ludwig-Maximilians-Universität for time resolved pump/probe experiments with attosecond resolution. High harmonic generation and subsequent filtering of the generated extreme ultraviolet (XUV) continuum by means of metal filters and XUV multilayer mirrors serve for the generation of isolated attosecond laser pulses. After high harmonic generation, the remaining fundamental laser pulse is spatially separated from the attosecond XUV pulse, to what is to our knowledge for the first time, by means of a perforated mirror in a Mach–Zehnder interferometer. Active stabilization of this interferometer guarantees the necessary temporal resolution for tracking attosecond dynamics in real time. As a proof-of-principle, photoelectron streaking experiments are performed and experimental techniques for their realization are summarized. Finally we highlight the potential of the presented beamline system for future experiments in comparison with previously demonstrated attosecond beamlines. © *2010 American Institute of Physics.* [doi:10.1063/1.3475689]

I. INTRODUCTION

To date, attosecond laser pulses are the shortest controllable events. They offer access to the time evolution of the fastest phenomena we are currently able to investigate. These attosecond pulses are generated by a frequency conversion of ultrashort, few-cycle laser pulses in the visible/near infrared range. Events evolving on attosecond time scales are electron dynamics in atoms,[1] solids,[2] and molecules.[3] Up to now, pump-probe experiments exploring the attosecond time scale have been performed with isolated extreme ultraviolet (XUV) attosecond pulses as short as 80 asec (Ref. 4) as pump and field gradients of few-cycle carrier-envelope-phase (CEP) stabilized femtosecond laser pulses as probe. The limitation on near infrared CEP-stabilized femtosecond laser pulses with an electric field gradient on an attosecond time scale as a precisely synchronized attosecond reference besides the attosecond XUV pulse has the following two reasons: first, the currently achievable attosecond-pulse energies prevent the utilization of 2 attosecond pulses as pump and probe pulses since the two photon absorption probability scales with the fifth to sixth power of the wavelength,[5] which means that it is extremely low for the XUV regime. Second, the attosecond pulse generation is based on high-order harmonic generation (HHG) of the few-cycle infrared femtosecond laser pulse. Up to now, the separation of the generated high harmonics from the remaining fundamental infrared light is problematic due to the lack of beam splitting optics conserving the short pulse duration and high pulse energy of both the XUV attosecond pulse and the infrared femtosecond pulse. In principle, the use of doughnut-shaped beam profiles after placing a circular block in the fundamental beam allows for the spatial separation of the generated high harmonics from the fundamental light, however, at the expense of a substantially reduced fundamental intensity.[6] For that reason, the present attosecond experimental systems rely on the collinear propagation of both the attosecond and the femtosecond pulse. This collinear setup has been realized in first-generation attosecond beamlines,[7,8] which have limited potential for further manipulating the fundamental laser pulse in order to extend the developed techniques toward the use of near UV pulses in combination with XUV pulses. As a consequence, real-time attosecond pump-probe experiments of electron dynamics with waveforms other than the fundamental near-infrared (NIR)-waveform were not possible. Accordingly, experiments in more complex systems such as small molecules consisting of only a few atoms were prevented due to their typically very low absorption cross section in the visible and NIR part of the electromagnetic spectrum.

So far, interferometer setups for attosecond pump-probe experiments are based on splitting the fundamental beam before HHG.[9,10] This comes to the expense of a substantial reduction of the XUV photon flux and photon energy since only a fraction of the fundamental pulse energy is used for HHG.

For the first time, the AS-2 Attosecond Beamline at the Joint Laboratory for Attosecond Physics of the Max-Planck-Institut für Quantenoptik and Ludwig-Maximilians-

[a]Author to whom correspondence should be addressed. Electronic mail: markus.fiess@mpq.mpg.de.

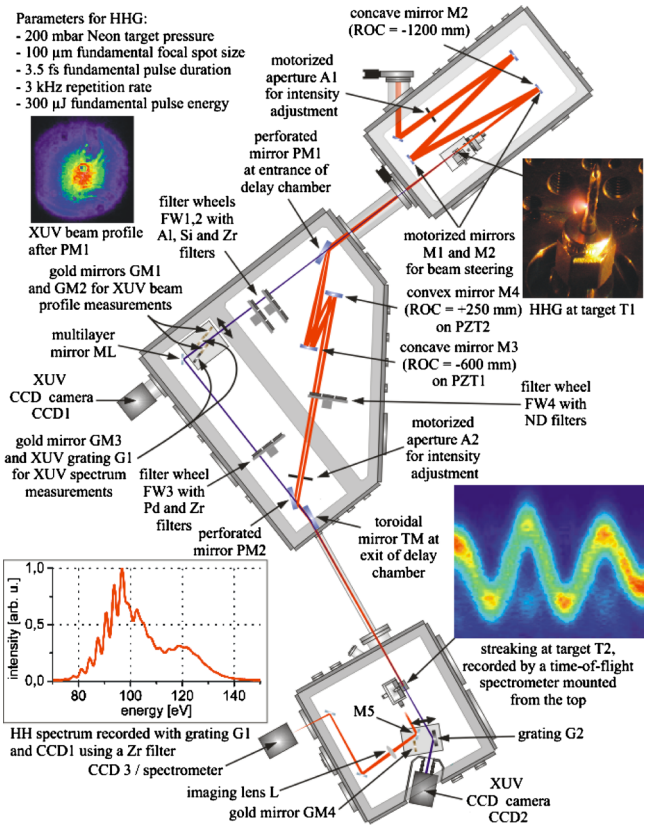

FIG. 1. (Color online) Experimental setup consisting of three vacuum chambers: chamber for HHG (top right), delay chamber (middle), and experiment chamber (bottom right).

Universität presented in this article allows for the spatial separation of the XUV attosecond laser pulse from the NIR femtosecond laser pulse after HHG. This feature opens the door for a conversion of the fundamental pulse to novel waveforms triggering a broad range of dynamics in different systems while using the full fundamental power for the generation of intense XUV pulses.

II. EXPERIMENTAL SETUP

Figure 1 shows the experimental setup: The laser system used for attosecond pulse generation is based on a commercial core (Femtolasers Produktions GmbH) adapted to the needs of the experiment. It generates CEP-stabilized laser pulses with 3.5 fs pulse duration, 300 μJ pulse energy at 3 kHz repetition rate, a spectrum spanning from 450 to 1050 nm with a central wavelength of 760 nm, and a vertical polarization.[11] Vertical polarization is more appropriate for designing XUV mirrors with high reflectance at non-normal incidence. These laser pulses, propagating in a vacuum system, are focused on a gas target T1 by a concave mirror M2, radius of curvature (ROC)=−1200 mm. The target consists of a nickel tube (3 mm diameter, 300 μm wall thickness, Good Fellow) filled with neon at a backing pressure of 200 mbar. In the 100 μm diameter focus, high harmonics with photon energies up to 140 eV are generated. Most of the optical components are motorized and can be adjusted under vacuum conditions: the flat mirror M1 and the concave mirror M2 in the HHG chamber are motorized for steering the direction of the beam. The gas target T1 can be moved in all three directions in space in order to position the gas target relative to the laser focus for optimum high harmonic generation. The movement along the beam axis allows to position the target into the part of the confocal parameter where preferably short-trajectory harmonics are generated.[12]

After HHG, both the generated high harmonic beam and the remaining fundamental light propagate collinearly into the second vacuum chamber, the delay chamber. Here, the fundamental light and the high harmonics are separated into the two paths of a Mach–Zehnder interferometer. One leg of the interferometer provides the possibility of adjusting the delay between the fundamental driving pulse and the generated attosecond pulse. The much smaller divergence of the high harmonic beam compared to the fundamental beam allows for the spatial separation of the two beams by means of a perforated mirror PM1, with a hole diameter of 1.0 mm through which the HH beam can pass. The distance between the target T1 and PM1 amounts to 900 mm. The fundamental light transmitted through the hole of PM1 is blocked by thin metal filters selected according to their transmittance (e.g., 500 nm Zr for the energy range of 70–140 eV, Lebow). These metal foils act as high pass filters for the high harmonic radiation. In combination with the reflectance characteristics of the multilayer mirror ML, a part of the HH spectrum is reflected. For few cycle laser pulses at a certain CEP the cutoff part of the continuum is smooth.[13] Filtering this region of the spectrum corresponds to the isolation of one single attosecond pulse out of an attosecond pulse train in the time domain.[14] HHG is optimized in terms of beam profile using an XUV sensitive camera [XUV camera PIXIS XO, Roper Scientific, charge-coupled device (CCD)1 in Fig. 1] and in terms of spectral distribution with a home-made grating spectrometer (grating 001–0266, Hitachi[15]). In order to preserve the interferometer stability, the multilayer mirror ML is not moved for beam profile measurements or spectral measurements of the generated HH. Instead, mirrors coated with 80% Au and 20% Pd (Georg Albert physical vapor deposition) on superpolished silicon substrates (Gooch & Housego) are moved in with a translation stage. At large incidence angles (>80°, measured from the normal axis resulting in a reflectance >60%) the HH radiation is reflected on two gold mirrors, bypassing the multilayer mirror, and is detected for beam profile measurements on a camera chip of an XUV CCD camera (CCD1 in Fig. 1). For spectral measurements the high harmonics are reflected off a third gold mirror, which can be inserted, and subsequently dispersed by a grating. The dispersed beam again circumvents the multilayer mirror and spectra are measured with the same XUV camera CCD1. For propagation of the HH to the experiment, all gold mirrors are moved out of the XUV beam.

The mirrors M3 and M4 in the other path of the Mach–Zehnder interferometer combine three functions:

(1) A telescope that consists of M3 (ROC=−600 mm) and M4 (ROC=+250 mm) for reducing the beam diameter.
(2) The delay between the fundamental pulse and the attosecond pulse in the other path of the interferometer is set by moving mirror M3, which is mounted on a

nanometer-resolution piezotranslation stage (PZT).

(3) Instabilities of the Mach–Zehnder interferometer are compensated by movements of mirror M4, which is mounted on a piezotranslation stage as well. M4 is the active part of a stabilization system of the interferometer, which is described in Sec. III.

The paths of both the fundamental beam and the high harmonics beam are recombined by a second perforated mirror PM2 with a hole diameter of 2.0 mm, which is approximately the XUV beam diameter at this point of the diverging XUV beam. The beams are subsequently focused on the experimental target T2 by a toroidal mirror TM (Société Européenne de Systèmes Optiques). The optical path length of the legs of the interferometer is 1700 mm. The distance between the second perforated mirror PM2 and the toroidal mirror is 100 mm. The toroidal mirror is coated with nickel, the angle of incidence is 86° measured from the normal axis, the effective focal length is 720 mm, and the accepted fundamental beam diameter is 6 mm. The divergence of the fundamental beam after the telescope formed by mirrors M3 and M4 is set such that the toroidal mirror TM focuses both the fundamental and the HH beam at the position of the experimental target T2. The distance between TM and T2 is 982 mm. The focal spot size of the fundamental focus generated by the toroidal mirror in the experiment chamber is 150 μm, and the maximum intensity is 5×10^{13} W/cm^2. The focal spot size of the XUV beam, measured with the knife-edge method, is 40 μm and therefore by a factor of 3 to 4 smaller than the focal spot size of the intense fundamental beam.

The experimental target T2 consists of a gas nozzle with motorized movement along all three dimensions. In pump-probe experiments, photoelectron spectra, ion mass spectra, and transient HH spectra can be measured for different delays between the fundamental pulse and the XUV pulse. Photoelectron spectra are recorded by means of an electron time-of-flight spectrometer (Stefan Käsdorf, Geräte für Forschung und Industrie) with an energy resolution of about 1% of the total kinetic photoelectron energy. The ion mass spectra are measured with a reflectron spectrometer (Stefan Käsdorf, Geräte für Forschung und Industrie).[16] Transient HH spectra can be measured with a second XUV-spectrometer after dispersion of the HH beam on grating G2 and detection of the spectra on CCD2 (grating 541 00 220, Jobin Yvon; XUV camera PIXIS XO, Roper Scientific).

Typical gas loads for HHG result in a pressure of 5×10^{-3} mbar in the HHG chamber. Differential pumping between the three vacuum chambers allows for a pressure of 5×10^{-4} mbar in the delay chamber and 8×10^{-6} mbar in the experiment chamber. The microchannel plate (MCP) detector of the electron time-of-flight spectrometer, which is mounted to the experiment chamber, is differentially pumped by a separate turbomolecular pump. The maximum gas load of the experimental target T2 is set such that the pressure of 3×10^{-6} mbar for neon as target sample is not exceeded in order to ensure safe operation of the MCP detector.

Summarizing all these features, four distinct advantages of the second generation attosecond beamline compared to its predecessors can be stated:

(1) The spatial separation of the fundamental light from the generated XUV light allows for a tailoring of the pump laser pulse according to the requirements of the experimental target, e.g., by nonlinear frequency conversion. In the previous attosecond beamlines[7,8] a manipulation of the remaining fundamental light after HHG was not possible due to the collinear propagation of fundamental light and XUV light after HHG.

(2) The angle of incidence on the flat multilayer mirror ML is 45°, which allows for mirror designs with significant higher reflectivity and larger spectral bandwidth for *s*-polarized XUV light as compared to near-normal incidence mirror designs as used in the previous attosecond beamlines.

(3) Focusing both the fundamental and the HH beam by means of a toroidal mirror at grazing incidence offers simultaneous access to transient absorption measurements and photoelectron streaking experiments at large XUV photon flux.

(4) A much longer Rayleigh range of both the fundamental and the XUV beam in the focus of the experimental target simplifies the alignment for streaking experiments considerably.

III. CALIBRATION OF THE XUV GRATING SPECTROMETER

The XUV spectrometers (G1 and G2) are calibrated using the absorption edges of aluminum and silicon foils. The XUV radiation is horizontally dispersed by the grating and the different wavelength components are recorded on the CCD-chip. Full vertical binning of the CCD chip results in raw spectra with the number of counts versus the pixel column number n. In the narrow wavelength range of interest it is a reasonable assumption that the pixel number n is proportional to the wavelength λ. The pixel number of the silicon absorption edge is n_1; the pixel number of the aluminum absorption edge is n_2. With this follows the corresponding wavelength λ for each pixel n

$$\lambda(n) = \frac{\lambda(n_1) - \lambda(n_2)}{n_1 - n_2}(n - n_2) + \lambda(n_2). \quad (1)$$

The conversion from wavelengths λ in nanometer to photon energies E in eV is calculated by $E(\mathrm{eV}) = 1239/\lambda(\mathrm{nm})$. Typical raw spectra recorded after transmission through thin aluminum, silicon, and zirconium foils and the corresponding calibrated XUV spectra are shown in Fig. 2.

IV. ALIGNMENT OF THE TEMPORAL AND SPATIAL OVERLAP

Finding the temporal overlap of the pump and the probe pulses is straightforward in a collinear setup like in the first generation attosecond beamline.[7,8] The metal filters, which block the fundamental light that propagates along the XUV beam path, are removed and two fundamental laser pulses

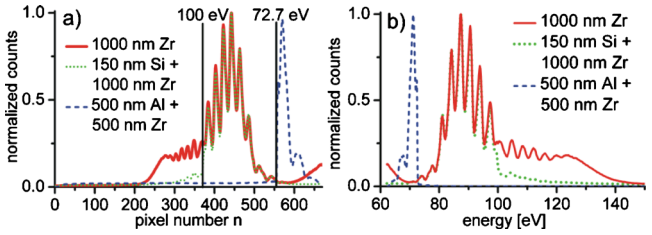

FIG. 2. (Color online) (a) Raw HH spectra and (b) calibrated HH spectra measured after transmission through thin metal foils made of Zr (solid line), Si (dotted line), and Al (dashed line). The spectrum below 70 eV in case of a 1000 nm zirconium filter shows the second diffraction order of the grating.

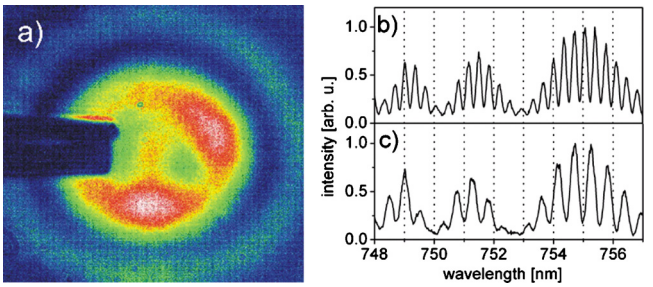

FIG. 3. (Color online) (a) Spatial interference with the shadow of the gas nozzle, (b) and (c) spectral interference of two fundamental laser pulses for (b) τ=5.4 ps and for (c) τ=3.5 ps.

are interfered in the focus of the experimental target. Each of the two laser pulses propagates along one of the two paths of the interferometer. A lens, which images the focus at the position of the experimental target through a glass window on a CCD-camera outside the vacuum chamber, is sufficient for the detection of the interference pattern between two fundamental laser pulses (CCD3 in Fig. 1). In case of a large interferometer setup, however, this method causes severe difficulties since the coherence length of the fundamental laser pulses amounts to only a few microns and determines the delay range within which this spatial interference is visible. Finding this micrometer-size overlap region in a Mach–Zehnder interferometer is nontrivial. Using a high-resolution spectrometer, one can observe the interference in the spectral domain over a much wider delay range. The same imaging system in combination with a spectrometer (HR4000, 0.05 nm resolution, Ocean Optics) instead of a CCD camera observes spectral fringes as follows:

Fourier transformation of the temporal electric field of two laser pulses

$$E_1(t) = \frac{1}{2}\left[\frac{1}{2\pi}\int_{\omega=-\infty}^{+\infty} d\omega\sqrt{I(\omega)}\exp(-i\omega t) + \text{c.c.}\right], \tag{2}$$

$$E_2(t) = \frac{1}{2}\left\{\frac{1}{2\pi}\int_{\omega=-\infty}^{+\infty} d\omega\sqrt{I(\omega)}\exp[-i\omega(t+\tau)] + \text{c.c.}\right\} \tag{3}$$

with identical spectrum $I(\omega)$, flat phase but delayed by τ, gives the modulated total spectrum

$$I_{\text{tot}}(\omega) = \left|\int_{t=-\infty}^{+\infty} dt[E_1(t) + E_2(t)]\exp(i\omega t)\right|^2$$

$$= 2I(\omega)[1 + \cos(\omega\tau)]. \tag{4}$$

The modulation of $I_{\text{tot}}(\omega)$ is determined by the delay τ between the two laser pulses. Since the number of fringes per frequency interval increases with τ, this method allows the definition of an increasing or decreasing delay if the delay is changed, e.g., by moving PZT1 in Fig. 1. In case of a central wavelength of 750 nm and a spectral resolution of 0.05 nm, delays of up to 38 ps corresponding to 11 mm difference of optical path length can be resolved.

A prerequisite for the observation of modulated spectra as shown in Figs. 3(b) and 3(c) is that the intensities of the two interfering laser pulses are of the same magnitude. Reducing the intensity of the more intense laser pulse by inserting a neutral density filter into the beam, e.g., with filter wheel FW4 in Fig. 1, is not a solution, since this filter would introduce additional group delay. Instead, the intensities are balanced by adjusting aperture A2 in Fig. 1. Closing aperture A2, however, slightly steers the beam path. Therefore, the spatial overlap of both laser beams at the position of target T2 is adjusted by moving in a neutral density filter with filter wheel FW4 and observing the image of the two foci on CCD camera CCD3 [Fig. 3(a)].

V. ACTIVE STABILIZATION OF THE MACH–ZEHNDER INTERFEROMETER

In the past, attosecond pump-probe experiments have been realized in collinear[7,8] and in Mach–Zehnder[9,10] interferometer setups. Pump-probe experiments with a temporal resolution on an attosecond timescale in an interferometer setup require nanometer-scale relative stability of the optical beam path lengths of the two paths, since temporal delays between the pump and the probe pulse are set by controlling the difference of the optical path lengths of both pulses. This can be ensured by an active feedback stabilization of the interferometer,[10,17] where the error signal is acquired in a reference interferometer. This reference interferometer is formed by half inch optical components mounted on top of those forming the XUV-IR interferometer. By attaching the components on the mounts that support the XUV-IR interferometer, we ensure that the behavior in terms of drift of the reference beam paths exactly mimic the drift motion of the beam paths of the fundamental and XUV laser pulses, which are used in the actual experiment. The thermal stability of the whole interferometer setup benefits from the use of stainless steel for most of the components due to its small thermal expansion coefficient in comparison with, e.g., aluminum.

In the following, the two beam splitters mounted on the two perforated mirrors are called BS1 and BS2. The half inch mirrors of the upper reference interferometer, which are the little brothers of ML, M3, and M4 in Fig. 1, are called stabilization mirrors SML, SM3, and SM4, respectively. A continuous-wave (cw) laser beam of a low noise, vacuum compatible diode laser (ULN diode laser, Coherent) is split into two beams by BS1, which is mounted on the mirror mount of PM1 in Fig. 1. Both beams are recombined by a second half inch beam splitter BS2, which is mounted on the mirror mount of PM2. The beam, which is transmitted by BS1 propagates above the beam path of the high harmonics

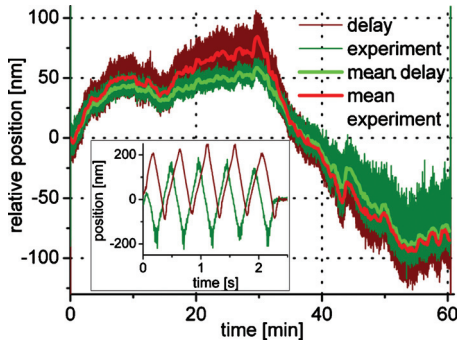

FIG. 4. (Color) Relative change of the optical path length of the reference interferometer (delay, red) and the lower interferometer, which has to be stabilized (experiment, green). The thick red and green lines show the mean value per second of both interferometers. The inset shows the calibration by means of a linear movement of the piezotranslation stage PZT2 before the active stabilization is started (see text).

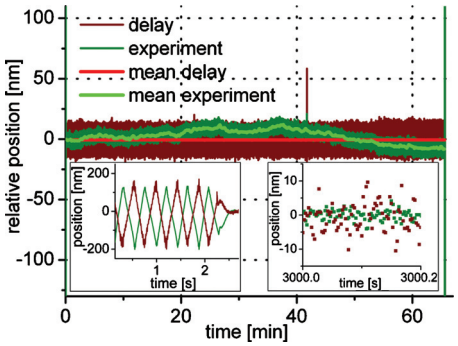

FIG. 5. (Color) Variation of the difference of the optical path length of the reference interferometer (delay, red) and the lower interferometer (experiment, green), in case of active stabilization. The thick red and green lines show the mean value per second of both interferometers. As in Fig. 4 the left inset shows the calibration by means of a linear movement of the piezostage PZT2 before the active stabilization is started. The right inset illustrates the statistical noise of 80 data points.

beam and is reflected by a half inch mirror SML attached on the mirror mount of ML in Fig. 1. Since M3 in Fig. 1 is used for controlling the delay between the fundamental laser pulse and the XUV laser pulse, M3 is not directly coupled with the reference interferometer. Instead, the mirror mount of M3 is mounted on a piezotranslation stage PZT1. PZT1 and the stainless steel post, on which the mount of the half inch mirror SM3 of the reference interferometer is installed, are assembled on the same base plate. M4 and SM4 are mounted on a second piezotranslation stage PZT2 (NanoX200CAP, Piezosystem Jena), which is used for the active stabilization of both the lower interferometer and the upper reference interferometer.

After BS2, the intensity of the interference between both cw beams of the reference interferometer is measured by means of a small active surface photodiode (silicon pin detector ET-2000, EOT). It is operated in photoconductive mode with an active area of only 80×80 μm^2 in order to avoid averaging over several interference fringes. A change of the intensity measured by the photodiode corresponds to a change of the difference of the optical path lengths of the two paths of the Mach–Zehnder interferometer. Therefore, the photodiode voltage was stabilized by means of a PID-algorithm written in LABVIEW and controls the voltage, which sets the position of piezotranslation stage PZT2. The PID-algorithm performs 400 corrections per second of the position of PZT2. The limiting factor for the speed of the active stabilization is the resonance frequency of PZT2 at approximately 500 Hz in case of a mass load of only 55 g for the mirrors M4, SM4, and their mounts. Therefore, only slow drifts due to thermal expansion of the breadboard, mirror mounts, etc. can be compensated but not fast vibrations introduced by, e.g., turbomolecular pumps. Such fast vibrations have been efficiently suppressed by using dampers between the turbomolecular pumps and the walls of the vacuum chambers, by a decoupling of the walls of the chamber and the optical table inside the delay chamber on which the interferometer is mounted, and by using turbomolecular pumps with magnetic bearings.

In order to test the quality of the coupling between both interferometers, a second cw laser was set up in the HHG chamber and propagated through the lower interferometer from the focus for HHG in the HHG chamber all the way up to the focus in the experiment chamber. The focus in the experiment chamber was imaged outside on a second photodiode identical to the one used for the reference interferometer in the delay chamber. Figure 4 shows the relative change of the optical path lengths in both the upper reference interferometer and the lower interferometer, which has to be actively stabilized. This measurement proves, first, that both interferometers are coupled with an accuracy of less than 15 nm and, second, that the observed long-term drift motion of more than 100 nm is not negligible and has to be compensated by means of an active stabilization.

Before the active stabilization is started and after the stabilization is stopped, PZT2 is moved linearly over a distance of several microns in order to generate some fringes, which are detected by the photodiode of the reference interferometer in the delay chamber. These fringes are used for the calibration of the changes of the path length from the measured photodiode voltages. The linear change of the photodiode voltage at the points of inflection of the sinusoidal curve is extrapolated to the minima and maxima and the photodiode voltage and converted to a path length change assuming a distance of $\lambda/2$ between adjacent extrema of the sinusoidal voltage curve. After this calibration, the sinusoidal voltage curve changes to a zigzag curve as stipulated by the linear movement of PZT2 (see inset of Figs. 4 and 5).

Figure 5 shows the same measurement as displayed in Fig. 4 in case of active stabilization of the Mach–Zehnder interferometer. It proves the capability of the presented stabilization scheme to suppress long term drift motions of the interferometer paths to within 50 as on a time scale of 1 h. The residual drift motion of the IR-XUV interferometer, which is shown in Fig. 5, might be due to imperfect coupling of both interferometers. For time intervals of 1 s, which is usually the minimum integration time for the data acquisition of, e.g., photoelectron spectra, the standard deviation has been calculated in case of the lower interferometer. The mean value of all standard deviations per 1 s interval is only 1.8 nm which corresponds to 6.0 as and defines the short term stability of the Mach–Zehnder interferometer. Different

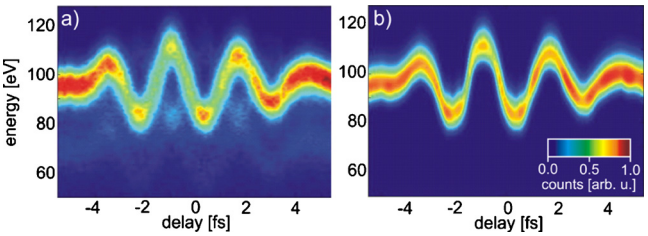

FIG. 6. (Color online) (a) Streaking spectrogram of $2p$ photoelectrons of neon measured with the active stabilization of the interferometer setup. The photoline at lower energies, which is hardly visible, originates from electrons released from the $2s$ orbital. It is suppressed due to the setting of the electrostatic lens of the electron time-of-flight spectrometer, which was optimized for highest $2p$ photoelectron count rate. (b) Retrieved streaking spectrogram after background subtraction and a FROG retrieval, which reproduces the streaking curve of the $2p$ photoelectrons.

electromagnetic shielding of the photodiodes and cables explains the different statistical noise for both interferometers.

VI. STREAKING MEASUREMENTS

The kinetic energy distribution of photoelectrons, which are released by XUV photons of an attosecond pulse, can be modified by the electric field of a synchronized and intense NIR laser pulse. A measurement of the kinetic energy of the photoelectrons for different delays between the XUV pulse and the NIR pulse is called "streaking", and the measured streaking curve can be approximately described by the vector potential of the NIR electric field.[18,19] A streaking measurement of the NIR electric field was performed to prove the functionality of the presented setup. Photoelectron spectra for different delays between the XUV and NIR pulse were recorded by focusing both the NIR and XUV beams in neon gas with simultaneous active stabilization of the Mach–Zehnder interferometer in the delay chamber. A typical streaking scan resulting from such a measurement is shown in Fig. 6(a).

The measured streaking curve shown in Fig. 6(a) proves the necessary short-term stability of the Mach–Zehnder interferometer in the delay chamber. The active stabilization of the interferometer setup guarantees the absence of such long-term drift motions as shown in Fig. 4 within the accuracy of the active stabilization. A long term drift motion would manifest itself as an apparent chirp of the NIR electric field in the streaking spectrogram. The obvious absence of a change in the periodicity of the sampled vector potential witnesses the reliability of the active stabilization.

In the presented data, the integration time per delay step was 10 s, the total acquisition time amounted to 15 min. The spectrogram was recorded using a XUV multilayer mirror supporting a bandwidth of 13 eV with a peak reflectance of 10% at 113 eV and a flat spectral phase. A 150 nm thick palladium foil was used as a high-pass filtering material. In the experiment, an electron time-of-flight spectrometer records the photoelectron flight time versus delay between the attosecond XUV pulse and the femtosecond NIR pulse. The maximum number of photoelectron counts per flight time channel of the electron time-of-flight spectrometer amounted to 814. Since one spectrum represents the sum over 30000 laser shots, multiple events resulting in detection nonlinearities can be safely excluded.

The conversion of the measured quantity of photoelectron counts $n_t(t)$ per flight time t to photoelectron counts $n_E(E)$ per kinetic energy E has to comply with the conservation of the total number of photoelectrons

$$\int_0^\infty n_t(t)dt = \int_\infty^0 n_E(E)dE \Leftrightarrow n_E\left[\frac{m}{2}\left(\frac{s}{t}\right)^2\right] = n_t(t)\frac{t^3}{ms^2}. \tag{5}$$

Here, m is the electron mass, t is the flight time, and s is the flight distance. This correction of the number of photoelectron counts was applied to the raw data of the spectrogram, as shown in Fig. 6(a).

For the measured streaking spectrogram of Fig. 6(a), the energy range of the electrostatic lens, within which the photoelectron count rate is increased by several orders of magnitude, was optimized for the kinetic energy of photoelectrons emitted from the $2p$ shell of the neon atoms. Therefore, the streaking curve generated by photoelectrons, which are emitted from the $2s$ shell of the neon atoms, is hardly visible at lower energies around 70 eV. Scattered photoelectrons produce a delay-independent background at photoelectron energies below the $2p$ streaking curve. Photoelectrons generated via above-threshold-ionization do not appear in the presented energy range for the laser intensities employed in the experiment. A small XUV satellite pulse containing ~12.5% of the total XUV power causes a weak $2p$ streaking curve, which is time-shifted by half a laser period with respect to the intense $2p$ streaking curve generated by the main XUV pulse. Due to this half-period shift, the minima of the $2p$ streaking curve caused by the XUV satellite pulse coincide with the maxima of the $2s$ streaking curve and are further accentuated by the background of scattered photoelectrons. Therefore, the minima and maxima of the weak $2p$ satellite streaking curve do not show the same number of photoelectron counts. The presence of a satellite pulse must manifest itself as a modulation of the XUV photon spectrum that leads to the according intensity modulation of the photoelectron spectra.[4] The spectral resolution of the electron time-of-flight spectrometer in the energy range of the presented data is not sufficient for resolving these spectral fringes. However, FROG requires streaking to be fully coherent. Therefore, the spectral fringes must be measured for the satellite pulse to be characterized. For this reason, the FROG algorithm has ignored the satellite pulse, which does not appear in the retrieved spectrogram, shown in Fig. 6(b).

The measured streaking spectrogram displayed in Fig. 6(a) clearly demonstrates that the attosecond pulses isolated from the XUV continuum carry no visible chirp, which would require an absolute GDD of about 5000 $asec^2$ to be resolved in the presented energy range. The FROG analysis, presented in Fig. 6(b), was performed after background subtraction of the measured streaking spectrogram, and reproduces the higher photoelectron count rates around each crest of the vector potential. In case of an unchirped XUV pulse, the peaking count rates for those delay steps is caused by the

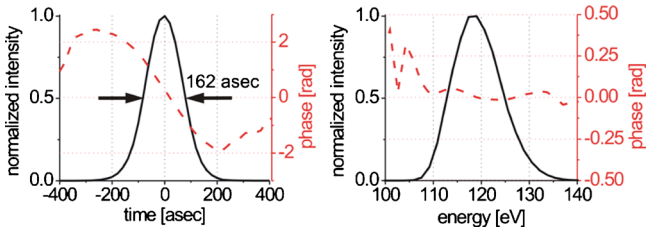

FIG. 7. (Color online) (a) Retrieved temporal intensity (solid line) and phase (dashed line) of the XUV pulse. (b) Retrieved spectrum (solid line) and spectral phase (dashed line) of the XUV pulse.

fact that the XUV ionization takes place when the vector potential is approximately constant within the XUV pulse duration. Since the change of the photoelectron momentum is proportional to the vector potential, this results in a minimal spectral broadening of the photoelectron spectra around the crests of the vector potential. The maximum count rate within the photoelectron bandwidth is therefore modulated along the delay axis even though the stability of the XUV source ensures an approximately constant ($\pm 3\%$) number of photoelectrons per delay step.

Figures 7(a) and 7(b) show the retrieved NIR electric field in the time domain and spectral domain, respectively. The analysis yields a flat spectral phase resulting in an average GDD of 240 asec^2 and a retrieved XUV pulse duration of 162 asec [full width at half maximum (FWHM)] close to the Fourier limit of 155 asec (FWHM). The FROG error $P=0.1694$ defines a measure of the difference between the background subtracted measured spectrogram with elements $A_{i,j}$, and the retrieved spectrogram with elements $B_{i,j}$, and indicates the accuracy of the FROG retrieval independent from the used array size. We define it as

$$P = \sqrt{\frac{2N}{N_1 + N_2}},$$
$$N = \sum_{i,j} (A_{i,j} - B_{i,j})^2, \quad N_1 = \sum_{i,j} A_{i,j}^2, \quad N_2 = \sum_{i,j} B_{i,j}^2. \tag{6}$$

The high reflectance of the XUV multilayer mirrors at the incidence angle of 45° results in a fivefold XUV photon flux, being quantified by a fivefold photoelectron count rate compared to previously demonstrated attosecond sources based on near normal incidence reflectors. This not only allows for quick scans to characterize both the XUV and the laser pulse but will also facilitate experiments that combine attosecond temporal resolution with samples that presently remained inaccessible due to their low absorption cross section, such as helium or secondary atomic emission lines. The resolution of attosecond cross-correlation experiments critically depends on the amplitude of the laser electric field used to streak the released photoelectrons.[20] In the presented setup, the long focal length used to focus the two beams results in a large volume with only small variations of the laser intensity and negligible Gouy-phase shift within the interaction region of the gas target and the laser beams. By virtue of this geometry, unprecedented ponderomotive modifications of the photoelectron kinetic energy are possible (as large as five times the spectral extend of the XUV pulse) and result in a very accurate pulse characterization.

VII. SUMMARY

In conclusion, we could show that our new second generation beamline allows the spatial separation of the remaining fundamental laser pulse from the generated HH after the HHG target. This enables a further manipulation of the fundamental laser pulse after HHG, for instance by nonlinear frequency conversion, and the preparation of a laser pulse suitable for an efficient interaction with various atomic or molecular target systems. The complication of the remaining instability of the interferometer setup could be solved by means of an active stabilization, which ensures the necessary long-term stability for pump-probe experiments with attosecond resolution. State-of-the-art streaking measurements with active stabilization of the interferometer demonstrate the feasibility of attosecond pump-probe experiments with this novel setup. Compared to previous attosecond beamlines both flux and spectral bandwidth of the XUV pulses could be increased by a 45° angle of incidence of the XUV beam on the reflecting multilayer optic. Future XUV sources will benefit from an extended reflectance ranging above 200 eV. Furthermore, this setup offers easy access to measurements of the transmitted XUV spectrum as a function of delay between the two pulses bringing attosecond transient absorption measurements into range.

ACKNOWLEDGMENTS

We thank B. Reiter, S. Köhler, M. Uiberacker, H. P. Schönauer, M. Fischer, A. Horn, and B. Horvath for support in setting up the beamline. This work was supported by the Munich Center for Advanced Photonics (MAP). R. Kienberger acknowledges funding from the Sofja Kovalevskaja Award of the Alexander von Humboldt foundation and an ERC Starting Grant. E.G. acknowledges a MC Reintegration Grant (Grant No. MERG-CT-2007-208643). M. Fieß is grateful to Studienstiftung des deutschen Volkes.

[1] M. Drescher, M. Hentschel, R. Kienberger, M. Uiberacker, V. Yakovlev, A. Scrinzi, Th. Westerwalbesloh, U. Kleineberg, U. Heinzmann, and F. Krausz, Nature (London) **419**, 803 (2002).
[2] A. L. Cavalieri, N. Müller, Th. Uphues, V. S. Yakovlev, A. Baltuska, B. Horvath, B. Schmidt, L. Blümel, R. Holzwarth, S. Hendel, M. Drescher, U. Kleineberg, P. M. Echenique, R. Kienberger, F. Krausz, and U. Heinzmann, Nature (London) **449**, 1029 (2007).
[3] B. H. Muskatel, F. Remacle, and R. D. Levine, Phys. Scr. **80**, 048101 (2009).
[4] E. Goulielmakis, M. Schultze, M. Hofstetter, V. S. Yakovlev, J. Gagnon, M. Uiberacker, A. L. Aquila, E. M. Gullikson, D. T. Attwood, R. Kienberger, F. Krausz, and U. Kleineberg, Science **320**, 1614 (2008).
[5] M. Schnürer, Z. Cheng, M. Hentschel, G. Tempea, P. Kálmán, T. Brabec, and F. Krausz, Phys. Rev. Lett. **83**, 722 (1999).
[6] J. Peatross, J. L. Chaloupka, and D. D. Meyerhofer, Opt. Lett. **19**, 942 (1994).
[7] M. Drescher, M. Hentschel, R. Kienberger, G. Tempea, C. Spielmann, G. A. Reider, P. B. Corkum, and F. Krausz, Science **291**, 1923 (2001).
[8] T. Pfeifer, M. J. Abel, P. M. Nagel, W. Boutu, M. J. Bell, Y. Liu, D. M. Neumark, and S. R. Leone, Opt. Lett. **34**, 1819 (2009).
[9] G. Sansone, E. Benedetti, F. Calegari, C. Vozzi, L. Avaldi, R. Flammini, L. Poletto, P. Villoresi, C. Altucci, R. Velotta, S. Stagira, S. De Silvestri, and M. Nisoli, Science **314**, 443 (2006).
[10] M. Chini, H. Mashiko, H. Wang, S. Chen, C. Yun, S. Scott, S. Gilbertson,

and Z. Chang, Opt. Express **17**, 21459 (2009).
[11] A. L. Cavalieri, E. Goulielmakis, B. Horvath, W. Helml, M. Schultze, M. Fieß, V. Pervak, L. Veisz, V. Yakovlev, M. Uiberacker, A. Apolonskiy, F. Krausz, and R. Kienberger, New J. Phys. **9**, 242 (2007).
[12] P. Antoine, A. L'Huillier, and M. Lewenstein, Phys. Rev. Lett. **77**, 1234 (1996).
[13] I. P. Christov, M. M. Murnane, and H. C. Kapteyn, Phys. Rev. Lett. **78**, 1251 (1997).
[14] M. Hentschel, F. Krausz, R. Kienberger, C. Spielmann, G. A. Reider, N. Milosevic, T. Brabec, P. Corkum, U. Heinzmann, and M. Drescher, Nature (London) **414**, 509 (2001).
[15] T. Kita, T. Harada, N. Nakano, and H. Kuroda, Appl. Opt. **22**, 512 (1983).
[16] M. Wagner and H. Schröder, Int. J. Mass Spectrom. Ion Process. **128**, 31 (1993).
[17] F. M. Böttcher, B. Manschwetus, H. Rottke, N. Zhavoronkov, Z. Ansari, and W. Sandner, Appl. Phys. B: Lasers Opt. **91**, 287 (2008).
[18] J. Itatani, F. Quéré, G. L. Yudin, M. Yu. Ivanov, F. Krausz, and P. B. Corkum, Phys. Rev. Lett. **88**, 173903 (2002).
[19] R. Kienberger, E. Goulielmakis, M. Uiberacker, A. Baltuska, V. Yakovlev, F. Bammer, A. Scrinzi, Th. Westerwalbesloh, U. Kleineberg, U. Heinzmann, M. Drescher, and F. Krausz, Nature (London) **427**, 817 (2004).
[20] J. Gagnon, E. Goulielmakis, and V. S. Yakovlev, Appl. Phys. B: Lasers Opt. **92**, 25 (2008).